# Witnessing nonequilibrium entanglement dynamics in a strongly correlated fermionic chain

Denitsa R. Baykusheva,[1] Mona H. Kalthoff,[2] Damian Hofmann,[2] Martin Claassen,[3] Dante M. Kennes,[4,2] Michael A. Sentef,[2] and Matteo Mitrano[1]

[1]*Department of Physics, Harvard University, Cambridge, Massachusetts 02138, USA*
[2]*Max Planck Institute for the Structure and Dynamics of Matter, Center for Free-Electron Laser Science (CFEL), Luruper Chaussee 149, 22761 Hamburg, Germany*
[3]*Department of Physics and Astronomy, University of Pennsylvania, Philadelphia, PA 19104, USA*
[4]*Institut für Theorie der Statistischen Physik, RWTH Aachen University, 52056 Aachen, Germany and JARA-Fundamentals of Future Information Technology, 52056 Aachen, Germany*

(Dated: September 7, 2022)

Many-body entanglement in condensed matter systems can be diagnosed from equilibrium response functions through the use of entanglement witnesses and operator-specific quantum bounds. Here, we investigate the applicability of this approach for detecting entangled states in quantum systems driven out of equilibrium. We use a multipartite entanglement witness, the quantum Fisher information, to study the dynamics of a paradigmatic fermion chain undergoing a time-dependent change of the Coulomb interaction. Our results show that the quantum Fisher information is able to witness distinct signatures of multipartite entanglement both near and far from equilibrium that are robust against decoherence. We discuss implications of these findings for probing entanglement in light-driven quantum materials with time-resolved optical and x-ray scattering methods.



*Introduction.*— A defining feature of quantum mechanics is the existence of nonlocal correlations (*entanglement*) among distinct physical objects [1, 2]. Entanglement is ubiquitous in the study of quantum many-body phenomena, encompassing areas such as quantum gravity [3], quantum information [4, 5], and condensed matter physics [6–11]. Especially in the latter, entanglement has significant effects on the macroscopic behavior of quantum materials [12, 13] and is intimately connected to the appearance of quantum spin liquidity [14–17], topological order [11, 16], quantum criticality [18], and strange metallic behavior [19, 20]. Therefore, efforts to identify and quantify quantum correlations in solids have the potential to reveal new collective phenomena and to advance our capability to harness their functionalities.

While small entangled systems can be experimentally characterized via tomography [21, 22] or quantum interference methods [23], diagnosing entanglement in solids requires alternative approaches linked to accessible experimental observables [6, 7, 24]. A possible strategy relies on determining the expectation values of operators called "entanglement witnesses" [13, 25–31]. The witness selection depends on the type of system and entanglement of interest, but a prominent quantity is the quantum Fisher information (QFI). At equilibrium, the QFI can be rigorously extracted from a sum-rule integral of the Kubo response function [32] and acts as a multipartite entanglement witness if its value exceeds classical expectations. Its connection with experimentally accessible response functions motivated recent inelastic neutron scattering studies of multipartite entanglement in a variety of spin chains [33–35] and defines a model-independent pathway to detect entangled states in quantum materials.

Witnessing entanglement with the QFI or other operators has significant implications well beyond the study of quantum systems at equilibrium. Recently, ultrafast laser pulses have enabled new pathways to drive quantum materials through nonequilibrium phase transitions, or induce entirely new states of matter without apparent equilibrium analogues [36–43]. Probing quantum entanglement for these dynamical phenomena is crucial in order to understand their microscopic origin and to identify the possible role of transient quantum coherence, especially in systems without obvious order parameters [44–47]. Hence, it becomes important to investigate how a time-dependent QFI reflects the evolution of entanglement through a nonequilibrium phase transition.

In this Letter, we show that the QFI is a robust witness of time-dependent multipartite entanglement across a prototypical nonequilibrium phase transition. We consider the experimentally relevant case of a fermion chain with a dynamically-tuned Coulomb repulsion [48–51] and map its entanglement dynamics for different driving conditions. Upon ramping the interaction strength, the system undergoes a quantum phase transition from a disordered to an ordered phase. The QFI witnesses an increase in multipartite entanglement while ramping the Coulomb interaction. For adiabatic ramps, the QFI exhibits a well-defined local maximum at the critical point, consistent with expectations for equilibrium quantum phase transitions [32]. By contrast, in a diabatic regime its increase persists deep into the ordered phase with distinctive oscillatory behavior. Crucially, such enhancement is robust against the introduction of local decoherence processes, thus underscoring the possibility to witness entanglement dynamics of quantum systems coupled to realistic dissipative baths. Our

results are immediately relevant to the nonequilibrium dynamics of one-dimensional Mott insulators in the strong coupling limit [e.g. $[Ni(chxn)_2Br]Br_2$, K-TCNQ, and (ET)-F2TCNQ] [48, 52–57], and, through a mapping onto an equivalent spin model, of spin chain systems such as $Cs_2CoCl_4$ [34], $KCuF_3$ [35], or $[Cu(\mu\text{-}C_2O_4)(4\text{-aminopyridine})_2(H_2O)]_n$ [33]. More broadly, our work defines a strategy to distinguish different dynamical regimes in driven materials via quantum information methods.

*Model.*— We consider a half-filled chain of spinless fermions interacting through a nearest-neighbor Coulomb repulsion. The model Hamiltonian reads,

$$\hat{\mathcal{H}}(t) = -\frac{J}{2}\sum_j (\hat{c}_j^\dagger \hat{c}_{j+1} + \text{H.c.}) + V(t)\sum_j \tilde{n}_j \tilde{n}_{j+1}, \quad (1)$$

where $\hat{c}_j^\dagger$ ($\hat{c}_j$) is a creation (annihilation) operator at site $j$, $\tilde{n}_j = \hat{c}_j^\dagger \hat{c}_j - 1/2$ is the number operator relative to half filling, and $J$ is a constant hopping amplitude setting the energy scale of our model. We consider a time-dependent nearest-neighbor Coulomb interaction $V(t)$, which can be realized in ultrafast optical experiments through dielectric screening enhancement [49], coherent Floquet dressing [43, 58], or transient crystal lattice distortions [59]. For simplicity, we ramp up the interaction strength at constant velocity as $V(t) = Jvt$. At equilibrium, this system exhibits a well-known quantum phase transition at $V = 1$ from a gapless Luttinger liquid (LL) with short-range correlations to a charge density wave (CDW) with long-range correlations.

We map the spinless fermions onto an equivalent spin-1/2 anisotropic Heisenberg chain (Fig. 1a) via a Jordan-Wigner transformation [60, 61] and add a small staggered magnetic field $h_z = 0.005$ (cf. Sec. S1 and S2 in the SM [62]) in order to select one of the two classical Néel states. We have checked that our key results are robust against the specific value of the field. We study the nonequilibrium entanglement dynamics through exact diagonalization (ED) calculations using the QuSpin [63, 64] and HPhi [65] packages. In the equivalent spin formulation, the quantum phase transition occurs between the XY and antiferromagnetic phases. The ED calculations for spin systems up to $L = 24$ sites are benchmarked for selected conditions against real-time density matrix renormalization group (DMRG) calculations [66] on an infinite fermionic chain.

We probe the entanglement dynamics by directly calculating the time-dependent QFI density using the instantaneous wavefunction describing the system. For a pure state $\psi_0$, the QFI associated with an operator $\hat{\mathcal{O}}_q$ is simply the connected correlation function [32]:

$$\mathcal{F}_Q = 4\Delta\left(\hat{\mathcal{O}}_q\right)^2 = 4\left(\langle\psi_0|\,\hat{\mathcal{O}}_q^2\,|\psi_0\rangle - \langle\psi_0|\,\hat{\mathcal{O}}_q\,|\psi_0\rangle^2\right). \quad (2)$$

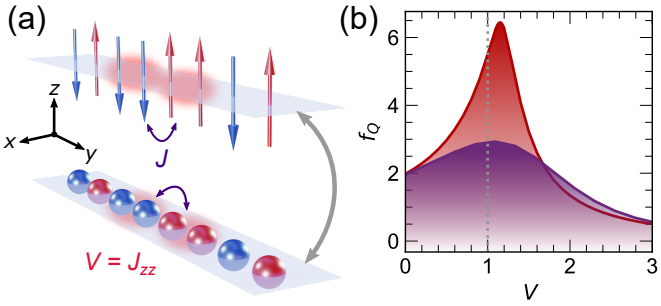


FIG. 1. (a) Sketch of half-filled spinless fermion chain with nearest-neighbor Coulomb interaction [Eq. (1)] (lower) and a corresponding spin-1/2 anisotropic Heisenberg model (upper). The fermionic hopping amplitude corresponds to the exchange coupling $J$ and the Hubbard interaction $V$ becomes the $z$-direction exchange coupling $J_{zz}$. (b) Equilibrium QFI density as a function of the intersite Coulomb repulsion $V$ computed using ED for a $L = 10$ chain (purple) and using DMRG for an infinite chain (red), respectively. If $f_Q > 1$, the system is at least bipartite entangled.

Since we focus on phase transitions to states with staggered correlations at wavevector $q = \pi$ [60], we choose the local generator $\hat{\mathcal{O}}_\pi = \sum_l (-1)^l \hat{S}_l^z$ (formulated in the spin language). A value of the QFI density $f_Q \equiv \mathcal{F}_Q/L > m$, where $m$ is a divisor of the system size $L$, signals that the state $|\psi_0\rangle$ must be $m+1$-partite entangled [30, 32].

*Results.*— Owing to the superposition of an increasing number of states due to quantum fluctuations, a system approaching a quantum phase transition will exhibit enhanced multipartite entanglement and a local QFI maximum at the critical point and for a finite temperature range [32]. We first investigate the evolution of the QFI density $f_Q$ upon tuning the interactions across the equilibrium critical point. As shown in Fig. 1b, $f_Q$ correctly identifies the quantum phase transition ($V = 1$) via a clear local maximum. This behavior is common to both the small and infinite-size limits (cf. Sec. S2 in [62]), whereby the chain length mainly determines the sharpness of the QFI maximum with minor effects on its exact position. In the gapless (LL) phase, the QFI density exceeds the classical bound $f_Q = 1$, thus witnessing at least bipartite entanglement. In the gapped (CDW) regime, the QFI density becomes featureless and decreases below the classical bound, thus signaling the absence of multipartite entanglement deep inside the ordered phase.

We now probe the nonequilibrium entanglement dynamics of our system. We consider a purely unitary evolution while ramping the interaction strength (see Fig. 2a). Starting from the noninteracting limit, we calculate the QFI of the time-evolved ground state $|\psi_0(t)\rangle = \mathcal{T}\exp\left[-i\int_{t_0}^t \hat{\mathcal{H}}(t')\mathrm{d}t'\right]|\psi_0(t_0)\rangle$ for a fine mesh

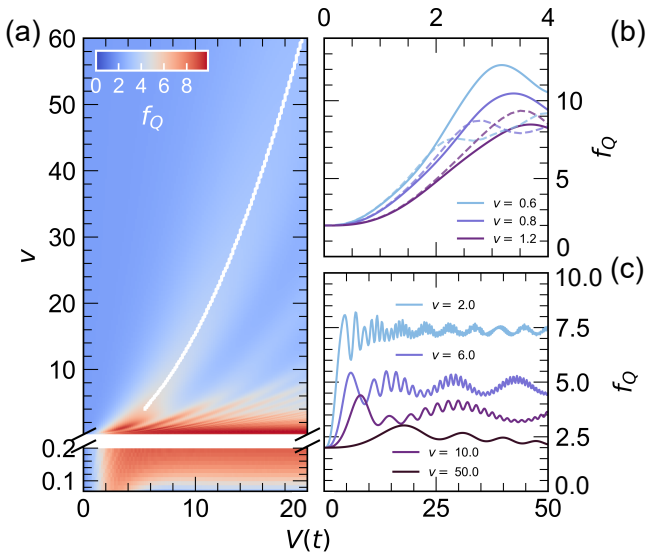


FIG. 2. (a) Nonequilibrium QFI density $f_Q = \mathcal{F}_Q/L$ as a function of time and ramp velocity for $L = 10$ sites. The white line marks the position of the instantaneous maxima of $f_Q$ in the impulsive region (see text). The lower part of the panel is a zoom of the quasi-adiabatic region. (b) Comparison between ED (dashed line) and DMRG (solid line) calculations of the time-dependent QFI density $f_Q$ for selected ramp velocities. (c) Time-dependent QFI density $f_Q$ for various ramp velocities.

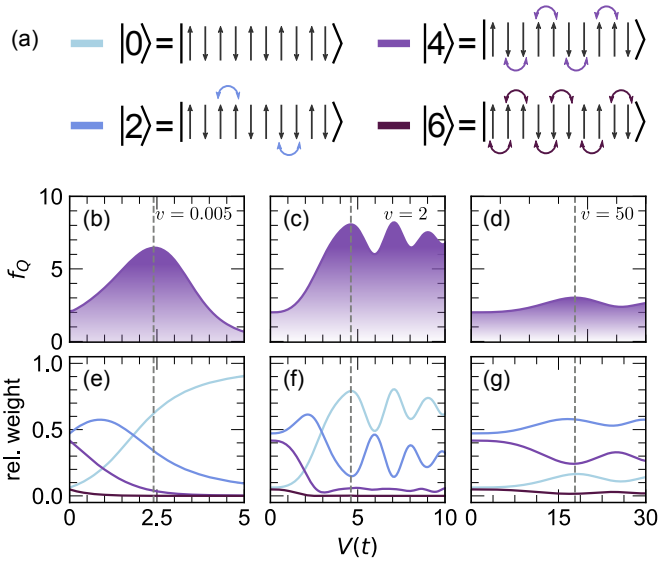


FIG. 3. Nonequilibrium QFI (top) and time-dependent density of defects (bottom) for selected velocities, (a),(d) $v = 0.005$, (b),(e) $v = 2$, and (c),(f) $v = 50$. Dashed vertical lines indicate the position of the first QFI maximum. (g) Chain configurations with a variable number of domain walls. The density of defects is given by the sum of the weights of time-evolved states containing zero to three domain walls.

of ramp velocities. In the adiabatic limit ($v \to 0$) the QFI density still peaks around the equilibrium quantum critical point. However, its nonequilibrium behavior exhibits significant differences. Upon increasing ramp speed, the local QFI maximum undergoes a long-lived enhancement with no signs of decay at large interaction strength. The transition to a diabatic regime occurs at relatively low velocity through a highly entangled state with $f_Q \sim L$. By decomposing the eigenstates of the instantaneous Hamiltonian into Fock states specifying the spins at each lattice site, we see that the entanglement growth of this region is mainly driven by a "Schrödinger-cat"-like superposition of nearly-degenerate Néel states $|\uparrow\downarrow\uparrow\downarrow \ldots\rangle$ and $|\downarrow\uparrow\downarrow\uparrow \ldots\rangle$ [67–80]. At higher ramp velocity ($v > 3.5$), the nonequilibrium enhancement of the QFI density peaks at larger interaction strengths (earlier times) and at a progressively lower level, thus suggesting a lower degree of multipartite entanglement. Intriguingly, the main peak of the time-dependent QFI density does not depend on system size (see Fig. 2b) or the presence of additional interaction terms in the equilibrium model (Sec. S6 in [62]). Hence, it represents a genuine nonequilibrium feature which does not extrapolate to the equilibrium critical point [81] and can be used to define a critical speed $v^*$ separating adiabatic and diabatic ('impulsive') dynamical regimes. In addition, the QFI density enhancement is accompanied by a characteristic oscillatory behavior (see Fig. 2c). These oscillations contain both size-dependent and size-independent frequency components, as analyzed in greater detail in Sec. S3 of the SM [62]. Through a time-frequency analysis via a sliding-window Fourier transform, we assign these oscillations to transitions across the gap of the instantaneous Hamiltonian $\omega(t) \approx \Delta(t)$ [82, 83].

To microscopically interpret the observed nonequilibrium entanglement dynamics, we decompose the instantaneous wavefunction $\psi_0(t)$ as a weighted superposition of Néel-like spin configurations with increasing number of domain walls (or *defects*, s. Fig. 3a). We then map the nonequilibrium QFI density at selected ramp velocities onto the time-dependent behavior of these weights (see Fig. 3). In the adiabatic limit ($v \lesssim 0.03$, see Fig. 3b, f), our system at $t_0 = 0$ is initialized in a disordered phase with a high density of defects. As the interaction strength grows, the time-evolved wavefunction $\psi_0(t)$ follows the ground state of the equilibrium Hamiltonian with effective interaction $V(t)$ and shows an increased superposition of pure Néel states without domain walls. Since the equally-weighted superposition of Néel states is maximally entangled and the underlying wavefunction cannot be represented as a product state, the QFI density $f_Q$ increases to a value close to the system size ($f_Q \sim L$). Then, above the transition into the ordered phase, $f_Q$ decays as the system selects one of the two Néel configurations and reduces the amount of multipartite

entanglement.

At small ramp velocities ($0.175 < v < 3.5$, see Fig. 3c, f), the entanglement dynamics becomes diabatic and involves the excitation of states with non-zero defect density. The system still features a growth of the superposition between pure Néel configurations with the QFI density $f_Q$ approaching the maximum value allowed by the system size. However, the departure from adiabaticity leads to the excitation of multiple low-lying states with a finite number of domain walls, their population being periodically redistributed as a function of time. At large ramp velocities ($v > 3.5$, see Fig. 3d, g), the QFI dynamics is deep in the diabatic regime. The time-evolved wavefunction does not follow the ground state evolution and its composition becomes skewed towards states with a non-zero number of domain walls. The superposition of pure Néel configurations is suppressed and the overall entanglement content of our model is reduced. In other words, a rapid change of the interaction strength drives the system into states with a larger number of defects and lower multipartite entanglement.

Since the QFI behavior is closely related to the proliferation of defects, we verify whether this entanglement witness follows a dynamics of the Kibble-Zurek (KZ) type [84, 85]. In the KZ picture, the dynamics of a system undergoing a quantum phase transition, including the scaling of the density of defects and other observables as a function of the quench velocity, is determined by its behaviour at the critical point [86–88]. While the validity of the KZ mechanism in the quantum regime has been established for trajectories across a critical point, our quench from the disordered to the ordered phase requires crossing an entire critical region ($0 \leq \Delta < 1$) [89, 90] and the critical point at $V = 1$ is of the Berezinskii-Kosterlitz-Thouless (BKT) type [91]. In the impulsive regime, we find that the nearest-neighbour Coulomb repulsion $V(t^*)$ maximizing the QFI density $f_Q$ is consistent with the KZ expectation and follows a dynamical scaling given by the power law $V(t^*) \propto v^\alpha$ with $\alpha \approx 1/2$ ($0.5295 \pm 0.0009$). In Sec. S5 of the SM [62], we relate $\alpha$ with the critical exponent of the system and the scaling of the gap at the critical point $V = 1$. Remarkably, for the systems sizes investigated here the KZ scaling of $V(t^*)$ is insensitive to diverse microscopic perturbations of the equilibrium model such as second-neighbor interactions, decoherence, or external fields [62].

Since most nonequilibrium experiments on condensed matter systems involve the coupling to an external environment, we now verify that the QFI density enhancement survives the presence of quantum dissipation. We evolve the density matrix $\hat{\rho}(t) = |\psi_0(t)\rangle\langle\psi_0(t)|$ according to a Lindblad master equation with a decoherence rate $\gamma$

$$\dot{\hat{\rho}}(t) = -i\left[\hat{\mathcal{H}}(t), \hat{\rho}(t)\right] + 2\gamma \sum_{l=0}^{L-1} \left(\hat{\mathcal{L}}_l \hat{\rho}(t) \hat{\mathcal{L}}_l^\dagger - \tfrac{1}{2}\left\{\hat{\mathcal{L}}_l^\dagger \hat{\mathcal{L}}_l, \hat{\rho}(t)\right\}\right). \quad (3)$$

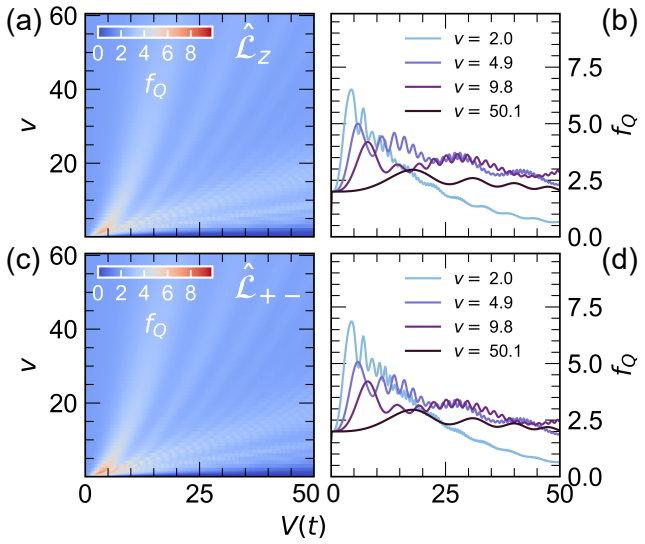


FIG. 4. Nonequilibrium QFI density $f_Q = \mathcal{F}_Q/L$ as a function of time and ramp velocity for $L = 10$ sites and at fixed decoherence rate $\gamma = 0.01$. (a),(c) Evolution of $f_Q$ in the presence of the Lindbladian jump operators $\hat{\mathcal{L}}_z$ and $\hat{\mathcal{L}}_{+-}$, respectively. (b),(d) Time-dependent $f_Q$ curves for selected ramp velocities.

We choose two different quantum jump operators $\hat{\mathcal{L}}_l$, namely $\hat{\mathcal{L}}_z \equiv \hat{\sigma}_l^z$ and $\hat{\mathcal{L}}_{+-} \equiv \hat{\sigma}_l^+ \hat{\sigma}_{l+1}^-$. The former describes local dephasing, relevant to the description of decay processes involving local degrees of freedom, such as molecular vibrations [55]. The latter encodes instead nonlocal quantum decoherence [92] relevant to systems featuring magneto-elastic coupling where the spin-exchange process is coupled to a bath of vibrational oscillators. The calculation of the QFI in this case follows a different prescription, as outlined in Sec. S4 in the SM [62]. As shown in Fig. 4, the decoherence terms suppress the "Schrödinger-cat"-like state at low ramp speeds and introduce a decay of the QFI density for increasing interaction strength. However, the main nonequilibrium QFI peak is preserved and persists up to coupling rates of $\gamma \approx 0.1$ [62] with only minor changes in location and magnitude. A decoherence rate $\gamma = 0.1$ is consistent with the experimental quasiparticle recombination rates of certain quasi-1D Mott insulators [55]. Hence, it should be possible to use the QFI density to witness nonequilibrium entanglement dynamics in realistic quantum systems subject to decoherence.

*Conclusion.*— We have investigated the nonequilibrium evolution of a driven fermion chain in terms of its many-body entanglement properties. By dynamically tuning the intersite Coulomb repulsion, we witness the multipartite entanglement dynamics with the time-dependent QFI across a prototypical quantum phase transition and find it robust against the introduction of

decoherence.

The existence of a rigorous connection between the QFI and the dynamical response of quantum systems at equilibrium has motivated recent attempts to witness multipartite entanglement in inelastic neutron scattering experiments [33–35]. The same protocols could be extended to certify the presence of entangled states in driven systems with ultrafast resonant inelastic x-ray scattering and optical methods. Although our work establishes the QFI as a valid nonequilibrium entanglement witness, further progress requires mapping the QFI operator to the transient response functions, thus abandoning the fluctuation-dissipation theorem as the key tenet of Ref. [32], and determining appropriate quantum bounds for the relevant observables. These two steps will allow extending the use of entanglement witnesses to future nonequilibrium spectroscopy experiments on quantum materials.

Our findings pave the way towards a deeper understanding of the role of quantum correlations in photoinduced phase transitions. The entanglement dynamics studied here is immediately relevant to laser-driven quasi-one-dimensional Mott insulators and spin chain materials [66] and represents a template to understand the more general behavior of correlated quantum materials out of equilibrium. In particular, entanglement correlations might allow for a better characterization of hitherto incompletely understood pathways towards hidden metastable phases [47, 93], the identification of dynamical quantum phases without obvious order parameters [94, 95], and could be key in unraveling the mystery behind light-induced phases of matter without equilibrium analogues [96].

We would like to thank S. R. Clark, J. Marino, Y. Wang, N. Yao, and P. Zoller for insightful discussions. M. M. acknowledges support by the Aramont Fellowship Fund for Emerging Science Research at Harvard University. D. R. B. was supported by the Swiss National Science Foundation through Project No. P400P2_194343. M. C. acknowledges support by NSF Grant No. DMR-2132591. D. M. K. acknowledges funding by the Deutsche Forschungsgemeinschaft (DFG, German Research Foundation) via Germany's Excellence Strategy – Cluster of Excellence Matter and Light for Quantum Computing (ML4Q) EXC 2004/1 – 390534769 and within the RTG 1995. M. A. S. acknowledges financial support through the Deutsche Forschungsgemeinschaft (DFG, German Research Foundation) via the Emmy Noether program (SE 2558/2). We also acknowledge support from the Max Planck-New York City Center for Non-Equilibrium Quantum Phenomena.

[1] J. S. Bell, *Speakable and Unspeakable in Quantum Mechanics. Collected Papers on quantum Philosophy* (Cambridge University Press, 1987).
[2] R. Horodecki, P. Horodecki, M. Horodecki, and K. Horodecki, Quantum entanglement, Rev. Mod. Phys. **81**, 865 (2009).
[3] T. Nishioka, S. Ryu, and T. Takayanagi, Holographic entanglement entropy: an overview, Journal of Physics A: Mathematical and Theoretical **42**, 504008 (2009).
[4] D. Bouwmeester, A. Ekert, and A. Zeilinger, *The Physics of Quantum Information* (Springer, 2000).
[5] M. A. Nielsen and I. L. Chuang, *Quantum Computation and Quantum Information* (Cambridge University Press, 2010).
[6] L. Amico, R. Fazio, A. Osterloh, and V. Vedral, Entanglement in many-body systems, Reviews of Modern Physics **80**, 517 (2008).
[7] V. Vedral, Quantifying entanglement in macroscopic systems, Nature **453**, 1004 (2008).
[8] N. Laflorencie, Quantum entanglement in condensed matter systems, Physics Reports **646**, 1 (2016).
[9] C. Gogolin and J. Eisert, Equilibration, thermalisation, and the emergence of statistical mechanics in closed quantum systems, Reports on Progress in Physics **79**, 056001 (2016).
[10] M. Ueda, Quantum equilibration, thermalization and prethermalization in ultracold atoms, Nature Reviews Physics **2**, 669 (2020).
[11] B. Zeng, X. Chen, D.-L. Zhou, and X.-G. Wen, *Quantum Information Meets Quantum Matter – From Quantum Entanglement to Topological Phase in Many-Body Systems* (Springer, New York, NY, 2019).
[12] S. Ghosh, T. F. Rosenbaum, G. Aeppli, and S. N. Coppersmith, Entangled quantum state of magnetic dipoles, Nature **425**, 48 (2003).
[13] Č. Brukner, V. Vedral, and A. Zeilinger, Crucial role of quantum entanglement in bulk properties of solids, Phys. Rev. A **73**, 012110 (2006).
[14] L. Balents, Spin liquids in frustrated magnets, Nature **464**, 199 (2010).
[15] L. Savary and L. Balents, Quantum spin liquids: a review, Reports on Progress in Physics **80**, 016502 (2016).
[16] X.-G. Wen, Colloquium: Zoo of quantum-topological phases of matter, Rev. Mod. Phys. **89**, 041004 (2017).
[17] G. Semeghini, H. Levine, A. Keesling, S. Ebadi, T. T. Wang, D. Bluvstein, R. Verresen, H. Pichler, M. Kalinowski, R. Samajdar, A. Omran, S. Sachdev, A. Vishwanath, M. Greiner, V. Vuletić, and M. D. Lukin, Probing topological spin liquids on a programmable quantum simulator, Science **374**, 1242 (2021).
[18] L. Prochaska, X. Li, D. C. MacFarland, A. M. Andrews, M. Bonta, E. F. Bianco, S. Yazdi, W. Schrenk, H. Detz, A. Limbeck, Q. Si, E. Ringe, G. Strasser, J. Kono, and S. Paschen, Singular charge fluctuations at a magnetic quantum critical point, Science **367**, 285 (2020).
[19] J. Zaanen, Planckian dissipation, minimal viscosity and the transport in cuprate strange metals, SciPost Phys. **6**, 61 (2019).
[20] S.-D. Chen, M. Hashimoto, Y. He, D. Song, K.-J. Xu, J.-F. He, T. P. Devereaux, H. Eisaki, D.-H. Lu, J. Zaanen, and Z.-X. Shen, Incoherent strange metal

sharply bounded by a critical doping in Bi2212, Science **366**, 1099 (2019).
[21] D. F. V. James, P. G. Kwiat, W. J. Munro, and A. G. White, Measurement of qubits, Phys. Rev. A **64**, 052312 (2001).
[22] H. Häffner, W. Hänsel, C. F. Roos, J. Benhelm, D. Chekal kar, M. Chwalla, T. Körber, U. D. Rapol, M. Riebe, P. O. Schmidt, C. Becher, O. Gühne, W. Dür, and R. Blatt, Scalable multiparticle entanglement of trapped ions, Nature **438**, 643 (2005).
[23] R. Islam, R. Ma, P. M. Preiss, M. Eric Tai, A. Lukin, M. Rispoli, and M. Greiner, Measuring entanglement entropy in a quantum many-body system, Nature **528**, 77 (2015).
[24] O. Gühne and G. Tóth, Entanglement detection, Physics Reports **474**, 1 (2009).
[25] V. Coffman, J. Kundu, and W. K. Wootters, Distributed entanglement, Phys. Rev. A **61**, 052306 (2000).
[26] L. Amico, A. Osterloh, F. Plastina, R. Fazio, and G. Massimo Palma, Dynamics of entanglement in one-dimensional spin systems, Phys. Rev. A **69**, 022304 (2004).
[27] T. Roscilde, P. Verrucchi, A. Fubini, S. Haas, and V. Tognetti, Studying Quantum Spin Systems through Entanglement Estimators, Phys. Rev. Lett. **93**, 167203 (2004).
[28] L. Amico, F. Baroni, A. Fubini, D. Patanè, V. Tognetti, and P. Verrucchi, Divergence of the entanglement range in low-dimensional quantum systems, Phys. Rev. A **74**, 022322 (2006).
[29] L. Pezzé and A. Smerzi, Entanglement, Nonlinear Dynamics, and the Heisenberg Limit, Phys. Rev. Lett. **102**, 100401 (2009).
[30] P. Hyllus, W. Laskowski, R. Krischek, C. Schwemmer, W. Wieczorek, H. Weinfurter, L. Pezzé, and A. Smerzi, Fisher information and multiparticle entanglement, Phys. Rev. A **85**, 022321 (2012).
[31] G. Tóth and I. Apellaniz, Quantum metrology from a quantum information science perspective, Journal of Physics A: Mathematical and Theoretical **47**, 424006 (2014).
[32] P. Hauke, M. Heyl, L. Tagliacozzo, and P. Zoller, Measuring multipartite entanglement through dynamic susceptibilities, Nature Publishing Group **12**, 778 (2016).
[33] G. Mathew, S. L. L. Silva, A. Jain, A. Mohan, D. T. Adroja, V. G. Sakai, C. V. Tomy, A. Banerjee, R. Goreti, A. V. N., R. Singh, and D. Jaiswal-Nagar, Experimental realization of multipartite entanglement via quantum Fisher information in a uniform antiferromagnetic quantum spin chain, Phys. Rev. Research **2**, 043329 (2020).
[34] P. Laurell, A. Scheie, C. J. Mukherjee, M. M. Koza, M. Enderle, Z. Tylczynski, S. Okamoto, R. Coldea, D. A. Tennant, and G. Alvarez, Quantifying and Controlling Entanglement in the Quantum Magnet $Cs_2CoCl_4$, Phys. Rev. Lett. **127**, 037201 (2021).
[35] A. Scheie, P. Laurell, A. M. Samarakoon, B. Lake, S. E. Nagler, G. E. Granroth, S. Okamoto, G. Alvarez, and D. A. Tennant, Witnessing entanglement in quantum magnets using neutron scattering, Phys. Rev. B **103**, 224434 (2021).
[36] W. Hu, S. Kaiser, D. Nicoletti, C. R. Hunt, I. Gierz, M. C. Hoffmann, M. Le Tacon, T. Loew, B. Keimer, and A. Cavalleri, Optically enhanced coherent transport in $YBa_2Cu_3O_{6.5}$ by ultrafast redistribution of interlayer coupling, Nature Materials **13**, 705 (2014).
[37] S. Kaiser, C. R. Hunt, D. Nicoletti, W. Hu, I. Gierz, H. Y. Liu, M. Le Tacon, T. Loew, D. Haug, B. Keimer, and A. Cavalleri, Optically induced coherent transport far above $T_c$ in underdoped $YBa_2Cu_3O_{6+\delta}$, Phys. Rev. B **89**, 184516 (2014).
[38] M. Mitrano, A. Cantaluppi, D. Nicoletti, S. Kaiser, A. Perucchi, S. Lupi, P. Di Pietro, D. Pontiroli, M. Riccò, S. R. Clark, D. Jaksch, and A. Cavalleri, Possible light-induced superconductivity in $K_3C_60$ at high temperature, Nature **530**, 461 (2016).
[39] M. Buzzi, D. Nicoletti, M. Fechner, N. Tancogne-Dejean, M. A. Sentef, A. Georges, T. Biesner, E. Uykur, M. Dressel, A. Henderson, T. Siegrist, J. A. Schlueter, K. Miyagawa, K. Kanoda, M.-S. Nam, A. Ardavan, J. Coulthard, J. Tindall, F. Schlawin, D. Jaksch, and A. Cavalleri, Photomolecular high-temperature superconductivity, Phys. Rev. X **10**, 031028 (2020).
[40] Y. H. Wang, H. Steinberg, P. Jarillo-Herrero, and N. Gedik, Observation of Floquet-Bloch States on the Surface of a Topological Insulator, Science **342**, 453 (2013).
[41] F. Mahmood, C.-K. Chan, Z. Alpichshev, D. Gardner, Y. Lee, P. A. Lee, and N. Gedik, Selective scattering between Floquet–Bloch and Volkov states in a topological insulator, Nature Physics **12**, 306 (2016).
[42] J. W. McIver, B. Schulte, F. U. Stein, T. Matsuyama, G. Jotzu, G. Meier, and A. Cavalleri, Light-induced anomalous Hall effect in graphene, Nature Physics **16**, 38 (2020).
[43] A. de la Torre, D. M. Kennes, M. Claassen, S. Gerber, J. W. McIver, and M. A. Sentef, Colloquium: Nonthermal pathways to ultrafast control in quantum materials, Rev. Mod. Phys. **93**, 041002 (2021).
[44] M. Claassen, H.-C. Jiang, B. Moritz, and T. P. Devereaux, Dynamical time-reversal symmetry breaking and photo-induced chiral spin liquids in frustrated Mott insulators, Nat. Comm. **8**, 1192 (2017).
[45] T. Kaneko, T. Shirakawa, S. Sorella, and S. Yunoki, Photoinduced $\eta$-Pairing in the Hubbard Model, Phys. Rev. Lett. **122**, 077002 (2019).
[46] F. Peronaci, O. Parcollet, and M. Schiró, Enhancement of local pairing correlations in periodically driven Mott insulators, Phys. Rev. B **101**, 161101 (2020).
[47] J. Li, D. Golez, P. Werner, and M. Eckstein, $\eta$-paired superconducting hidden phase in photodoped Mott insulators, Phys. Rev. B **102**, 165136 (2020).
[48] R. Singla, G. Cotugno, S. Kaiser, M. Först, M. Mitrano, H. Y. Liu, A. Cartella, C. Manzoni, H. Okamoto, T. Hasegawa, S. R. Clark, D. Jaksch, and A. Cavalleri, THz-Frequency Modulation of the Hubbard $U$ in an Organic Mott Insulator, Phys. Rev. Lett. **115**, 187401 (2015).
[49] N. Tancogne-Dejean, M. A. Sentef, and A. Rubio, Ultrafast Modification of Hubbard $U$ in a Strongly Correlated Material: Ab initio High-Harmonic Generation in NiO, Phys. Rev. Lett. **121**, 097402 (2018).
[50] S. Beaulieu, S. Dong, N. Tancogne-Dejean, M. Dendzik, T. Pincelli, J. Maklar, R. P. Xian, M. A. Sentef, M. Wolf, A. Rubio, L. Rettig, and R. Ernstorfer, Ultrafast dynamical Lifshitz transition, Science Advances **7**, eabd9275 (2021).
[51] D. R. Baykusheva, H. Jang, A. A. Husain, S. Lee, S. F. R. TenHuisen, P. Zhou, S. Park, H. Kim, J.-K. Kim, H.-

D. Kim, M. Kim, S.-Y. Park, P. Abbamonte, B. J. Kim, G. D. Gu, Y. Wang, and M. Mitrano, Ultrafast Renormalization of the On-Site Coulomb Repulsion in a Cuprate Superconductor, Phys. Rev. X **12**, 011013 (2022).

[52] S. Iwai, M. Ono, A. Maeda, H. Matsuzaki, H. Kishida, H. Okamoto, and Y. Tokura, Ultrafast Optical Switching to a Metallic State by Photoinduced Mott Transition in a Halogen-Bridged Nickel-Chain Compound, Phys. Rev. Lett. **91**, 057401 (2003).

[53] H. Okamoto, H. Matsuzaki, T. Wakabayashi, Y. Takahashi, and T. Hasegawa, Photoinduced Metallic State Mediated by Spin-Charge Separation in a One-Dimensional Organic Mott Insulator, Phys. Rev. Lett. **98**, 037401 (2007).

[54] H. Uemura, H. Matsuzaki, Y. Takahashi, T. Hasegawa, and H. Okamoto, Ultrafast Charge Dynamics in One-Dimensional Organic Mott Insulators, Journal of the Physical Society of Japan **77**, 113714 (2008).

[55] M. Mitrano, G. Cotugno, S. R. Clark, R. Singla, S. Kaiser, J. Stähler, R. Beyer, M. Dressel, L. Baldassarre, D. Nicoletti, A. Perucchi, T. Hasegawa, H. Okamoto, D. Jaksch, and A. Cavalleri, Pressure-Dependent Relaxation in the Photoexcited Mott Insulator ET $-$ $F_2$TCNQ: Influence of Hopping and Correlations on Quasiparticle Recombination Rates, Phys. Rev. Lett. **112**, 117801 (2014).

[56] S. Wall, D. Brida, S. R. Clark, H. P. Ehrke, D. Jaksch, A. Ardavan, S. Bonora, H. Uemura, Y. Takahashi, T. Hasegawa, H. Okamoto, G. Cerullo, and A. Cavalleri, Quantum interference between charge excitation paths in a solid-state Mott insulator, Nature Physics **7**, 114 (2011).

[57] N. Sono, T. Otaki, T. Kitao, T. Yamakawa, D. Sakai, T. Morimoto, T. Miyamoto, and H. Okamoto, Phonon-dressed states in an organic Mott insulator, Communications Physics **5**, 72 (2022).

[58] J. H. Mentink, K. Balzer, and M. Eckstein, Ultrafast and reversible control of the exchange interaction in Mott insulators, Nature Communications **6**, 6708 (2015).

[59] A. S. Disa, T. F. Nova, and A. Cavalleri, Engineering crystal structures with light, Nature Physics **17**, 1087 (2021).

[60] T. Giamarchi, *Quantum physics in one dimension*, International series of monographs on physics (Clarendon Press, Oxford, 2004).

[61] A. Altland and B. D. Simons, *Condensed matter field theory* (Cambridge University Press, 2010).

[62] See Supplemental Material for details on finite size effects, time-frequency and Kibble-Zurek analysis of the nonequilibrium QFI, and for additional details about the Lindbladian evolution.

[63] P. Weinberg and M. Bukov, QuSpin: a Python Package for Dynamics and Exact Diagonalisation of Quantum Many Body Systems. Part I: spin chains, SciPost Phys. **2**, 003 (2017).

[64] P. Weinberg and M. Bukov, QuSpin: a Python Package for Dynamics and Exact Diagonalisation of Quantum Many Body Systems. Part II: bosons, fermions and higher spins, SciPost Phys. **7**, 20 (2019).

[65] M. Kawamura, K. Yoshimi, T. Misawa, Y. Yamaji, S. Todo, and N. Kawashima, Quantum lattice model solver HΦ, Computer Physics Communications **217**, 180 (2017).

[66] D. M. Kennes, A. de la Torre, A. Ron, D. Hsieh, and A. J. Millis, Floquet Engineering in Quantum Chains, Phys. Rev. Lett. **120**, 127601 (2018).

[67] D. M. Greenberger, M. A. Horne, and A. Zeilinger, Going beyond bell's theorem, in *Bell's Theorem, Quantum Theory and Conceptions of the Universe*, edited by M. Kafatos (Springer Netherlands, Dordrecht, 1989) pp. 69–72.

[68] L. Pezzè, A. Smerzi, M. K. Oberthaler, R. Schmied, and P. Treutlein, Quantum metrology with nonclassical states of atomic ensembles, Rev. Mod. Phys. **90**, 035005 (2018).

[69] A. Ekert, R. Jozsa, R. Penrose, R. Laflamme, E. Knill, W. H. Zurek, P. Catasti, and S. V. S. Mariappan, NMR Greenberger-Horne-Zeilinger states, Philosophical Transactions of the Royal Society of London. Series A: Mathematical, Physical and Engineering Sciences **356**, 1941 (1998).

[70] P. Neumann, N. Mizuochi, F. Rempp, P. Hemmer, H. Watanabe, S. Yamasaki, V. Jacques, T. Gaebel, F. Jelezko, and J. Wrachtrup, Multipartite entanglement among single spins in diamond, Science **320**, 1326 (2008).

[71] D. Bouwmeester, J.-W. Pan, M. Daniell, H. Weinfurter, and A. Zeilinger, Observation of Three-Photon Greenberger-Horne-Zeilinger Entanglement, Phys. Rev. Lett. **82**, 1345 (1999).

[72] J.-W. Pan, M. Daniell, S. Gasparoni, G. Weihs, and A. Zeilinger, Experimental demonstration of four-photon entanglement and high-fidelity teleportation, Phys. Rev. Lett. **86**, 4435 (2001).

[73] X.-L. Wang, Y.-H. Luo, H.-L. Huang, M.-C. Chen, Z.-E. Su, C. Liu, C. Chen, W. Li, Y.-Q. Fang, X. Jiang, J. Zhang, L. Li, N.-L. Liu, C.-Y. Lu, and J.-W. Pan, 18-qubit entanglement with six photons' three degrees of freedom, Phys. Rev. Lett. **120**, 260502 (2018).

[74] D. Leibfried, E. Knill, S. Seidelin, J. Britton, R. B. Blakestad, J. Chiaverini, D. B. Hume, W. M. Itano, J. D. Jost, C. Langer, R. Ozeri, R. Reichle, and D. J. Wineland, Creation of a six-atom "Schrödinger cat" state, Nature **438**, 639 (2005).

[75] T. Monz, P. Schindler, J. T. Barreiro, M. Chwalla, D. Nigg, W. A. Coish, M. Harlander, W. Hänsel, M. Hennrich, and R. Blatt, 14-qubit entanglement: Creation and coherence, Phys. Rev. Lett. **106**, 130506 (2011).

[76] N. Friis, O. Marty, C. Maier, C. Hempel, M. Holzäpfel, P. Jurcevic, M. B. Plenio, M. Huber, C. Roos, R. Blatt, and B. Lanyon, Observation of entangled states of a fully controlled 20-qubit system, Phys. Rev. X **8**, 021012 (2018).

[77] L. DiCarlo, M. D. Reed, L. Sun, B. R. Johnson, J. M. Chow, J. M. Gambetta, L. Frunzio, S. M. Girvin, M. H. Devoret, and R. J. Schoelkopf, Preparation and measurement of three-qubit entanglement in a superconducting circuit, Nature **467**, 574 (2010).

[78] C. Song, K. Xu, W. Liu, C.-p. Yang, S.-B. Zheng, H. Deng, Q. Xie, K. Huang, Q. Guo, L. Zhang, P. Zhang, D. Xu, D. Zheng, X. Zhu, H. Wang, Y.-A. Chen, C.-Y. Lu, S. Han, and J.-W. Pan, 10-qubit entanglement and parallel logic operations with a superconducting circuit, Phys. Rev. Lett. **119**, 180511 (2017).

[79] B. Vlastakis, G. Kirchmair, Z. Leghtas, S. E. Nigg, L. Frunzio, S. M. Girvin, M. Mirrahimi, M. H. Devoret, and R. J. Schoelkopf, Deterministically Encoding Quantum Information Using 100-Photon Schrödinger Cat States, Science **342**, 607 (2013).

[80] A. Omran, H. Levine, A. Keesling, G. Semeghini, T. T. Wang, S. Ebadi, H. Bernien, A. S. Zibrov, H. Pichler, S. Choi, J. Cui, M. Rossignolo, P. Rembold, S. Montangero, T. Calarco, M. Endres, M. Greiner, V. Vuletić, and M. D. Lukin, Generation and manipulation of Schrödinger cat states in Rydberg atom arrays, Science **365**, 570 (2019).

[81] N. Tsuji, M. Eckstein, and P. Werner, Nonthermal Antiferromagnetic Order and Nonequilibrium Criticality in the Hubbard Model, Phys. Rev. Lett. **110**, 136404 (2013).

[82] F. Pollmann, S. Mukerjee, A. G. Green, and J. E. Moore, Dynamics after a sweep through a quantum critical point, Phys. Rev. E **81**, 020101 (2010).

[83] E. Canovi, E. Ercolessi, P. Naldesi, L. Taddia, and D. Vodola, Dynamics of entanglement entropy and entanglement spectrum crossing a quantum phase transition, Phys. Rev. B **89**, 104303 (2014).

[84] T. W. B. Kibble, Topology of cosmic domains and strings, Journal of Physics A: Mathematical and General **9**, 1387 (1976).

[85] W. H. Zurek, Cosmological experiments in superfluid helium?, Nature **317**, 505 (1985).

[86] A. Polkovnikov, Universal adiabatic dynamics in the vicinity of a quantum critical point, Phys. Rev. B **72**, 161201 (2005).

[87] W. H. Zurek, U. Dorner, and P. Zoller, Dynamics of a Quantum Phase Transition, Phys. Rev. Lett. **95**, 105701 (2005).

[88] J. Dziarmaga, Dynamics of a Quantum Phase Transition: Exact Solution of the Quantum Ising Model, Phys. Rev. Lett. **95**, 245701 (2005).

[89] R. Schützhold, M. Uhlmann, Y. Xu, and U. R. Fischer, Sweeping from the Superfluid to the Mott Phase in the Bose-Hubbard Model, Phys. Rev. Lett. **97**, 200601 (2006).

[90] F. Pellegrini, S. Montangero, G. E. Santoro, and R. Fazio, Adiabatic quenches through an extended quantum critical region, Phys. Rev. B **77**, 140404 (2008).

[91] M. Dalmonte, J. Carrasquilla, L. Taddia, E. Ercolessi, and M. Rigol, Gap scaling at Berezinskii-Kosterlitz-Thouless quantum critical points in one-dimensional Hubbard and Heisenberg models, Phys. Rev. B **91**, 165136 (2015).

[92] V. Eisler, Crossover between ballistic and diffusive transport: the quantum exclusion process, Journal of Statistical Mechanics: Theory and Experiment **2011**, P06007 (2011).

[93] V. Vedral, High-temperature macroscopic entanglement, New Journal of Physics **6**, 102 (2004).

[94] H.-C. Jiang, Z. Wang, and L. Balents, Identifying topological order by entanglement entropy, Nature Physics **8**, 902 (2012).

[95] A. Szasz, J. Motruk, M. P. Zaletel, and J. E. Moore, Chiral Spin Liquid Phase of the Triangular Lattice Hubbard Model: A Density Matrix Renormalization Group Study, Physical Review X **10**, 21042 (2020).

[96] J. Tindall, F. Schlawin, M. Buzzi, D. Nicoletti, J. R. Coulthard, H. Gao, A. Cavalleri, M. A. Sentef, and D. Jaksch, Dynamical order and superconductivity in a frustrated many-body system, Phys. Rev. Lett. **125**, 137001 (2020).

# Supplementary Material for: Witnessing nonequilibrium entanglement dynamics in a strongly correlated fermionic chain

Denitsa R. Baykusheva,[1] Mona H. Kalthoff,[2] Damian Hofmann,[2] Martin Claassen,[3] Dante M. Kennes,[4,2] Michael A. Sentef,[2] and Matteo Mitrano[1]

[1] *Department of Physics, Harvard University, Cambridge, Massachusetts 02138, USA*
[2] *Max Planck Institute for the Structure and Dynamics of Matter, Center for Free-Electron Laser Science (CFEL), Luruper Chaussee 149, 22761 Hamburg, Germany*
[3] *Department of Physics and Astronomy, University of Pennsylvania, Philadelphia, PA 19104, USA*
[4] *Institut für Theorie der Statistischen Physik, RWTH Aachen University, 52056 Aachen, Germany and JARA-Fundamentals of Future Information Technology, 52056 Aachen, Germany*

(Dated: September 7, 2022)

## S1. MODEL SYSTEM

In this work, we map a half-filled chain of spinless fermions interacting through nearest neighbor Coulomb repulsion onto a corresponsing spin Hamiltonian. The initial model Hamiltonian is given by:

$$\hat{\mathcal{H}}(t) = -\frac{J}{2}\sum_j (\hat{c}_j^\dagger \hat{c}_{j+1} + \text{H.c.}) + V(t)\sum_j \tilde{n}_j \tilde{n}_{j+1}, \tag{1}$$

where $\hat{c}_j^\dagger$ ($\hat{c}_j$) is a fermionic creation (annihilation) operator at site $j$, $\tilde{n}_j = \hat{c}_j^\dagger \hat{c}_j - 1/2$ is the number operator relative to half filling, $J$ is a constant hopping amplitude, and $V(t)$ is a time-dependent, nearest-neighbor Coulomb interaction. Through the Jordan-Wigner transformation [1], this charge Hamiltonian maps onto an equivalent spin-1/2 anisotropic Heisenberg (XXZ) chain (Fig. 1a in the main text):

$$\hat{\mathcal{H}}_{\text{sp}}(t) = \sum_j \left[ -\frac{J}{2}\left(\hat{S}_j^+ \hat{S}_{j+1}^- + \text{H.c.}\right) + V(t)\hat{S}_j^z \hat{S}_{j+1}^z \right], \tag{2}$$

where $\hat{S}_j^\pm = \frac{1}{2}\left(\hat{S}_j^x \pm \hat{S}_j^y\right)$ and $\hat{S}_j^\alpha$ ($\alpha = x, y, z$) are the usual spin operators defined in terms of the Pauli matrices $\hat{S}^\alpha = \frac{1}{2}\hat{\sigma}_\alpha$. In this picture, the hopping amplitude $J$ becomes the exchange coupling while $\Delta(t) = V(t)/J$ quantifies the anisotropy of the spin interactions.

At equilibrium, this dual quantum chain exhibits well-known quantum phase transitions. Upon increasing $\Delta = V/J$, the fermionic chain evolves from a gapless Luttinger liquid (LL) phase with short-range correlations to a charge density wave (CDW) phase with long-range correlations. The XXZ chain instead undergoes two separate transitions into an Ising ferromagnet ($\Delta < -1$) and antiferromagnet ($\Delta > 1$), while for ($|\Delta| < 1$) it exhibits an XY phase [1]. Since the dual charge and spin formulations are one-to-one equivalent, we choose to study the time-dependent dynamics of the quantum spin chain using exact diagonalization (ED). The ED calculations for finite-size chains extending up to $L = 24$ sites are performed using the QuSpin [2, 3] as well as the HPhi [4] packages.

The antiferromagnetic XXZ ground state in a finite-size system contains a mixture of nearly-degenerate states (notably $|\uparrow\downarrow \ldots \uparrow\downarrow\rangle \pm |\downarrow\uparrow \ldots \downarrow\uparrow\rangle$). In order to break this near degeneracy, which turns into complete degeneracy in the thermodynamic limit, we also introduce a small staggered magnetic field $\hat{\mathcal{H}}_{\text{ext}} = \sum_j (-1)^j h_z \hat{S}_j^z$ to select a specific spin configuration (cf. next section). This ensures that the disconnected part of the spin correlation function in Eq. (2) in the main text vanishes in the limit $\Delta \to \infty$. Our spin sector quench dynamics is then benchmarked for selected conditions against real-time density matrix renormalization group (DMRG) calculations [5] of the time evolution of an infinite chain.

## S2. FINITE-SIZE EFFECTS ON THE QUANTUM FISHER INFORMATION CALCULATIONS

In the antiferromagnetic (AFM) Ising limit $\Delta \to \infty$, the ground state of the XXZ chain in the spin sector is degenerate in the thermodynamic limit ($L \to \infty$) and is given by the two possible Néel states $|\uparrow\downarrow\uparrow\downarrow \ldots\rangle$ and $|\downarrow\uparrow\downarrow\uparrow \ldots\rangle$, related to each other via a site translation. At finite $L$, the two lowest-energy spin configurations $|\uparrow\downarrow\uparrow\downarrow \ldots\rangle \pm |\downarrow\uparrow\downarrow\uparrow \ldots\rangle$ are split by a finite energy gap that decreases as $\propto e^{-\alpha L}$ with increasing system size (with $\alpha > 0$). For the AFM

ground state at finite $L$, the disconnected part of the spin correlation function in Eq. (2) of the main text, i.e. $\sum_l (-1)^l \left\langle \hat{S}^z_l \right\rangle \left\langle \hat{S}^z_{l+1} \right\rangle$, vanishes, leading to an asymptotically finite value of the QFI $F_Q$. In order to reinstate the proper behaviour of the QFI certified by the DMRG calculations in the charge sector, we introduce a staggered degeneracy-breaking magnetic field term $\hat{\mathcal{H}}_{\text{ext}} = \sum_j (-1)^j h_z \hat{S}^z_j$ to select a specific Néel component of the ground state and restore the proper limit of $F_Q$. Consequently, the position of the maximum of the equilibrium QFI density shown in Fig. 1b of the main text thus becomes dependent on the magnitude $h_z$ of this additional term. In addition, both the magnitude of the QFI maximum as well as its position are dependent on the chain length $L$. In Fig. S1, we plot the equilibrium QFI density in the spin sector as a function of the staggered magnetic field for a fixed chain length (panel a) and as a function of the system size for a fixed $h_z$.

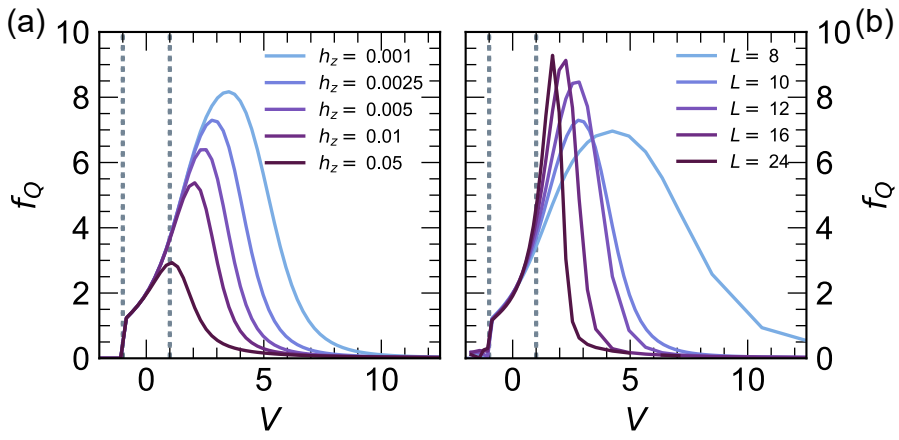


FIG. S1. (a) Equilibrium QFI density $f_Q$ for a spin chain with $L = 10$ for different values of the staggered magnetic field $h_z$. (b) QFI density as a function of the chain length for a fixed $h_z = 1.414$.

## S3. TIME-FREQUENCY ANALYSIS OF THE NON-EQUILIBRIUM QFI

In Fig. 2 of the main text and the accompanying discussion, we outline the main features of the nonequilibrium QFI dynamics. Upon crossing the critical point $\Delta = 1$, the driven system passes through a more entangled state compared to the initial condtion. Depending on the ramp velocity, the QFI density $f_Q(t) = F_Q(t)/L$ either maps onto the equilibrium phase diagram, thereby decaying asymptotically to zero as $t \to \infty$, or exhibits a rich oscillatory behaviour when the driving protocol reaches the impulsive limit at sufficiently high velocities. In this section, we focus on origin of the oscillatory dynamics, while the transition between adiabatic and impulsive regimes is discussed in Sec. S5.

We start by focusing our attention on the 1D linecuts of $f_Q(t)$ plotted in Fig. 2c of the main text. In panel a of Fig. S2, we present three of these curves as a function of physical time instead of the time-dependent nearest-neighbour Coulomb repulsion $V(t)$. Both representations are related through the transformation $t = V(t)/v$. The time-domain representation allows us to better appreciate characteristic dynamical features of the non-adiabatic regime ($v > 3.5$). First, all curves in Fig. S2a reveal a slow oscillation at $\nu_{\text{osc}} \sim 0.36$, independent of the driving speed. Furthermore, all curves also contain very fast oscillations, evident at early times and featuring a pronounced chirp. In order to isolate the different frequency contributions and characterize the change of the non-stationary contributions as a function of time, we perform a short-time Fourier transform (STFT) analysis. In the resulting spectrogram, a stationary frequency manifests itself as a horizontal line, whereas a linear change of the frequency over time corresponds to a linear chirp.

In panels b-d of Fig. S2, we plot the spectrograms corresponding to the three velocities $v = 2.0$, $v = 10.0$, and $v = 40.0$. The $v$-independent oscillations correspond to the low-frequency mode at $\nu_{\text{osc}} \sim 2\pi\Delta_{01} \approx 0.36$. The fast oscillations show a linear chirp, more clearly pronounced at faster ramp velocities, with a slope given by $\bar{b} \sim \frac{v}{2\pi}$.

We now discuss the microscopic origin of these features with the aid of Fig. S3. By analyzing the energy level diagram of the $L = 10$ chain (with $h_z$ fixed at 0.005), we can attribute the $\nu_{\text{osc}} \sim 0.36$ oscillation to a transition

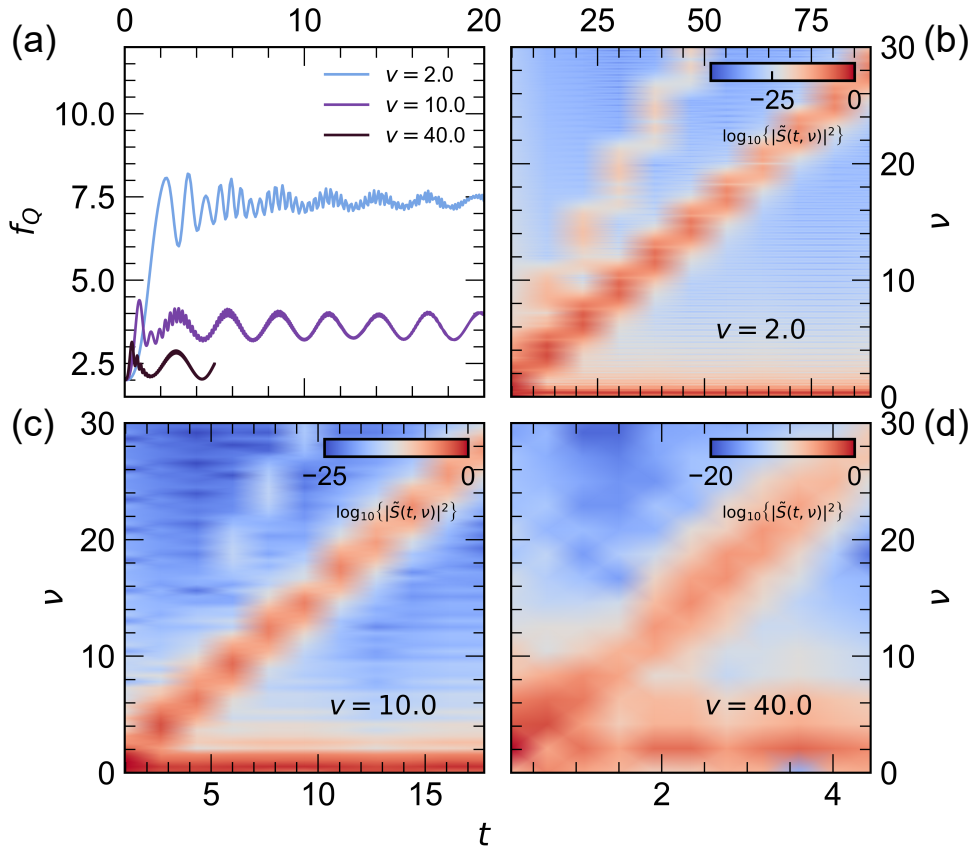


FIG. S2. (a) Linecuts from Fig. 2c in the main text, plotted as a function of time. (b) - (d) spectrograms of the time-dependent QFI density for three selected velocities: $v = 2$ (b), $v = 10$ (c), and $v = 40$ (d). Note that the color scale is logarithmic.

between the ground and the first excited level. The corresponding energy separation $\Delta_{01}$ is shown as a function of the nearest-neighbour Coulomb repulsion for different chain sized in Fig. S3a. For $L = 10$ and sufficiently large anisotropies ($\Delta > 3$), the gap size assumes an asymtoptic value of $\frac{0.314}{2\pi}$, hence, the oscillation frequency in the spectrograms in Fig. S2 is largely time-independent.

The second dominant feature, the linearly-chirped rapid oscillations, has its origin in a transition between the ground state and one of the higher-lying excited levels ($j = 5$). The corresponding gap $\Delta_{05}$ increases linearly with $V$ (see Fig. S3b), its slope for $L = 10$ matches well the slope of the corresponding feature in the short-time Fourier transform. The relationship between the two is $\frac{b}{v} \sim \frac{1}{2\pi}\frac{\mathrm{d}\Delta_{05}}{\mathrm{d}V}$. The excitation to this (and others) specific state(s) occurs while driving the system through the critical point $\Delta = 1$. In panel c of Fig. S3, we plot the projection of the time-evolved initial pure state $\psi_0(t)$ (coinciding with the GS of the LL-model at $t_0 = 0$) onto the $j^{\mathrm{th}}$-eigenstate of the time-dependent Hamiltonian $\hat{\mathcal{H}}(t)$ (denoted by $\psi_t^{(j)}$) at the *end of the time evolution* $t_{\max}$. Apart from the nearly-degenerate low-lying states with $j = 1, 2$, only the state with $j = 5$ has a significant contribution, and beatings with the $\psi_0(t)$ dominate the time-frequency structure of the non-equilibrium QFI. The state $\psi_t^{(j=5)}$ is dominated by spin configurations featuring two domain walls (e.g. $|\uparrow\uparrow\downarrow\uparrow\uparrow\downarrow\uparrow\downarrow\uparrow\downarrow\rangle$) for all values of $t$, whereas the time-evolved $\psi_0(t)$, especially after crossing $\Delta = 1$, becomes progressively dominated by the defect-free two Nèel configurations. The projection of $\psi_0(t)$ onto the initial state at $t_0$, plotted as a dark purple line in Fig. S3c, exhibits an interesting dynamics consisting of a decay followed by multiple revivals. For completeness, in panel d of the same figure we show the temporal evolution of several matrix elements $b_{ij} = \left\langle \psi_t^{(i)} \right| \left|\psi_0(t)\right\rangle \left\langle \psi_0(t)\right| \left|\psi_t^{(j)}\right\rangle$, i.e. the projection of $\psi_0(t)$ over the instantaneous eigenstate at each $t$. These results imply that the non-equilibrium QFI in the impulsive regime is determined by the non-adiabatic excitation of multiple states at the critical point and the associated increased domain wall density.

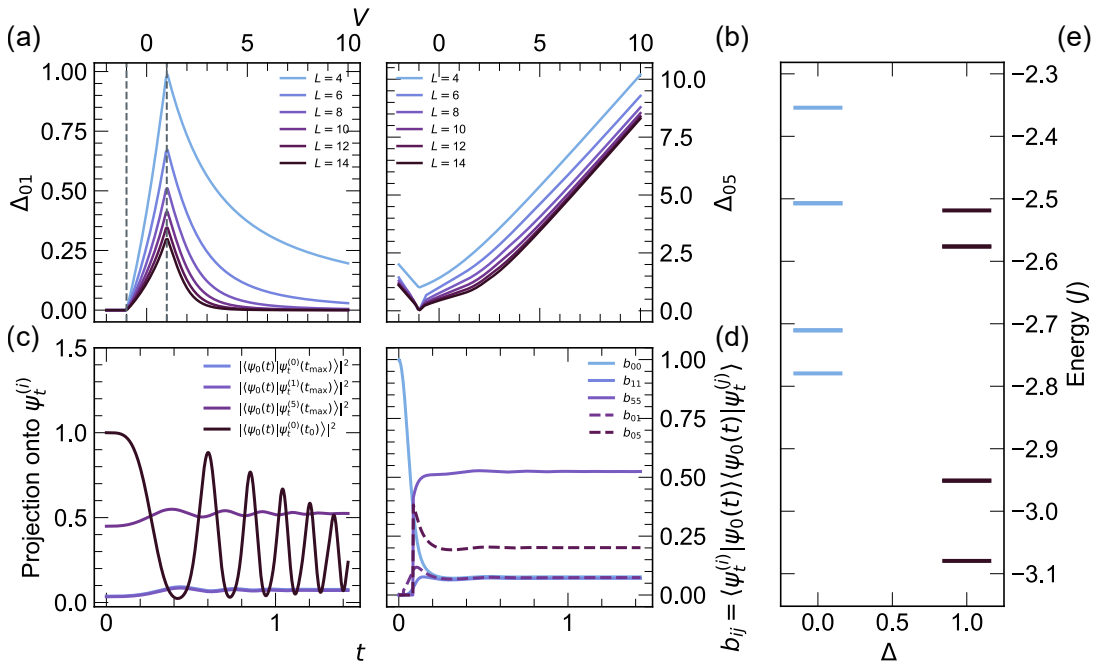


FIG. S3. (a)-(b) Energy separations between the ground state and the first (a) resp. the fifth (b) excited states of the chain, plotted as a function of the nearest-neighbour Coulomb repulsion for different chain lengths. A staggered magnetic field value of $h_z = 0.005$ has been used. Grey vertical lines in (a) indicate the positions of the critical points. (c) Projection of the time-evolved state $\psi_0(t)$ onto selected eigenstates of the *time-dependent* Hamiltonian at the end of the time-evolution $\hat{\mathcal{H}}(t = t_{\max})$. The dark-purple curve shows the projection of $\psi_0$ onto the initial state at $t_0$. Panel (d) Time-dependence of selected matrix elements $b_{ij}$, given by products of overlaps of the time-propagated $\psi_0(t)$ with the eigenstates of the *instantaneous* Hamiltonian $\hat{\mathcal{H}}(t)$ at time $t$. Panel (e) energy diagram showing the relevant energy levels dominating the dynamics. Some of the energy levels are degenerate.

## S4. LINDBLAD MASTER EQUATION

In Fig. S4, we present calculation results showcasing the influence of the decoherence rate on the QFI during non-unitary time evolution ($L = 10$, $h_z = 0.005$). The main features are preserved for coupling strengths up to $\gamma \sim 0.05$, and become progressively obliterated as $\gamma \geq 0.1$. The dissipative Lindblad jump operator acting on each site $l$ is given by $\hat{\mathcal{L}}^{(l)} \equiv \hat{\mathcal{L}}_z = \hat{\sigma}_l^z$.

The QFI in the presence of decoherence is calculated by first propagating the density matrix $\hat{\rho}(t)$ obeying the initial condition:

$$\hat{\rho}(t_0) = |\psi_0(t_0)\rangle \langle\psi_0(t_0)| \,. \tag{3}$$

The QFI is obtained as [6]:

$$\mathcal{F}_Q(t) = 2 \sum_{i,j} \frac{\left(\epsilon_t^i - \epsilon_t^j\right)^2}{\epsilon_t^i + \epsilon_t^j} \left|\langle\varphi_t^i| \hat{\mathcal{O}}_\pi |\varphi_t^j\rangle\right|^2 , \tag{4}$$

where $\epsilon_t^i$ and $|\varphi_t^i\rangle$ are the eigenvalues and the eigenvectors of $\hat{\rho}$ at time $t$.

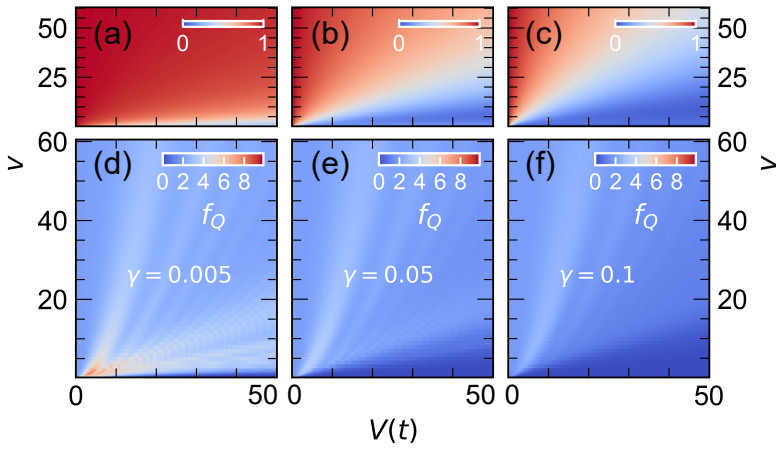


FIG. S4. (a)-(c) Density matrix purity as a function of effective nearest-neighbour Coulomb repulsion and ramp speed. The decoherence rate is set to $\gamma = 0.005$ in panels (a)/(d), to $\gamma = 0.05$ in (b)/(e), and to $\gamma = 0.1$ in (c)/(f). (d)-(f) Non-equilibrium QFI in the presence of decoherence for three different decoherence rates $\gamma$, displayed as a function of the effective nearest-neighbour Coulomb repulsion and ramp speed. The colormap is normalized with respect to the unitary QFI density, shown in Fig. 2a of the main text.

## S5. KIBBLE-ZUREK ANALYSIS OF THE NONEQUILIBRIUM QFI

The nonequilibrium QFI dynamics (see. Fig. 2a of the main text) of the spinless fermion chain subject to a linear ramp can be broadly divided into three regions depending on the ramp velocity. These regimes can be delineated by tracking the the time ($t^*$) or the effective nearest-neighbour Coulomb interaction ($V(t^*)$) which maximize the time-dependent $f_Q$ at a given ramp speed $v$. The resulting curve (s. white line in Fig. 2a or Fig. S5a-c) effectively tracks the position of the main QFI "crest" as it propagates towards larger $V(t^*)$ (smaller $t^*$) on increasing the ramp speed. The positions of the maxima are extracted by fitting a skewed Voigt distribution to the time profile of $f_Q$ at each velocity in a region centered around the main peak.

The two limiting cases are defined by the adiabatic ($v < 0.025$, cf. Fig. S5a) and the nonadiabatic ($v > 3.5$, cf. Fig. S5b-c) limits, separated by an intermediate region. Whereas the onset of the non-adiabatic region is rather sudden and well-marked by a "kink" in the $v - V(t^*)$ resp. $v - t^*$ plots in Fig. S5b-c, the separation between adiabatic and intermediate regions is rather fluid. In the deep adiabatic regime, the position of the $f_Q$-maximum is weakly dependent on the driving speed, and the driven system essentially traces out the equilibrium phase diagram. This regime (illustrated for $v = 0.001$ in Fig. S5d) holds as long as excitations to the first excited state on crossing the critical point $\Delta = 1$ can be neglected, i.e. $b_{ij} \approx \delta_{0,i}\delta_{0,j}$ for the entire time evolution. Examining the time-resolved data underlying Fig. 2a, we estimate a value of $v^{*,1} \sim 0.025$ for the maximum ramp speed that warrants purely adiabatic evolution before oscillations due to excitations to the first excited state develop. Invoking simple Landau-Zener (LZ) arguments, we can estimate the corresponding excitation probability to the first excited state as $P_{01} = 1 - e^{-\frac{\pi\tilde{\delta}\Delta_{01}^2}{2v}}$, where $\tilde{\delta}$ is a constant related to the rate of change of the gap at $\Delta = 1$ as a function of the critical parameter $V(t)$. The threshold for the breakdown of adiabaticity in the LZ picture ($\Delta_{01}^2 \approx v|\mathrm{d}\Delta_{01}/\mathrm{d}V|$), however, largely overestimates $v^{*,1}$, indicating a more complex behaviour.

For ramp velocities above $v^{*,1}$ but not exceeding $v^{*,2}$, the dynamics falls into the intermediate regime, characterized by an extensive scaling of the QFI density $f_Q \sim L$ in the unitary evolution case. Due to the rapidly oscillating and saturating behaviour of $f_Q$, the corresponding maxima could not be extracted for velocities ranging from 0.175 up to shortly before the onset of the non-adiabatic region $v^{*,2} \sim 3.5$ (cf. square/diamond symbols in Fig. S5b-c). Here, the dynamics are mainly governed by the ground and the first excited states of the system, as one can deduce from the dominant $b_{ij}$-coefficients in Fig. S5e. Recalling that in the presence of the staggered magnetic field of amplitude $h_z$ the ground state at $t_0$ is dominated by one of the two Néel configurations, creating excitations across the gap mixes the wavefunction with the state where the other Néel is dominant. The resulting superposition contains these two components with a similar amplitude, hence the growth of the entanglement.

The non-adiabatic regime has a sharply delineated onset, marked by a rapid change of the slopes of $\Delta v/\Delta V(t^*)$

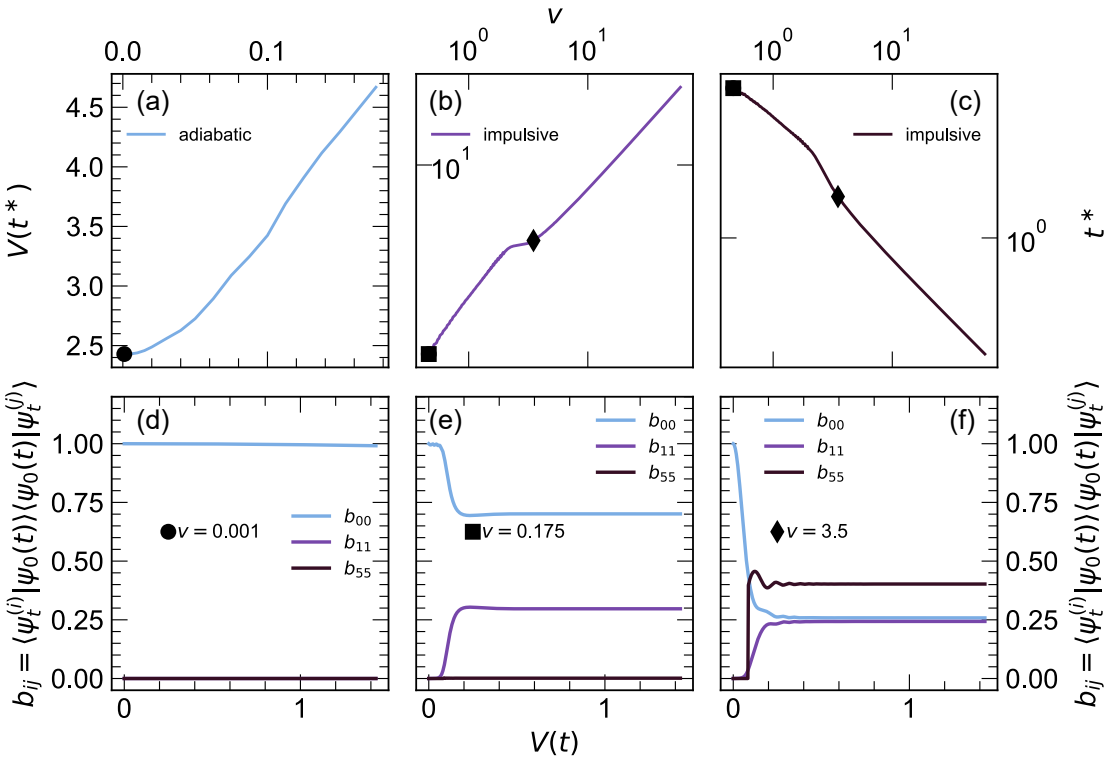


FIG. S5. (a)-(c) Positions of the maxima of the time-dependent QFI density $f_Q$ as a function of the ramp velocity, displayed as a function of the effective nearest-neighbour Coulomb repulsion [panels (a) and (b)] or time (c). Points falling into the adiabatic and (partially) to the "intermediate" regime are shown in panel (a). Panels (b) and (c) show the "intermediate" and the non-adiabatic regions on a double-logarithmic scale. The onset of the non-adiabatic regime is manifested by a marked change in the slope of the curves (see text). The symbols indicate the positions of the three different ramp velocities corresponding to the data in the bottom row. (d)-(f) Time-dependent matrix elements $b_{ij}$, given by products of overlaps of the time-propagated $\psi_0(t)$ with the eigenstates of the *instantaneous* Hamiltonian $\hat{\mathcal{H}}(t)$ at time $t$, shown for three different velocities (see legends).

resp. $\Delta v/\Delta t^*$. The nonadiabatic limit commences when the probability of an excitation to the higher-lying states (in particular $j = 5$ for the $L = 10$ chain) exceeds the corresponding excitation fraction to the first excited state $j = 1$ (cf. Fig. S5f), leading to proliferation of defects. In this regime, the maximum of the QFI density follows a regular behaviour, and its functional dependence can be extracted by fitting the corresponding slopes in Fig. S5b-c: $V(t^*) \propto \sqrt{v}$ resp. $t^* \propto v^{-1/2}$. The exact values of the slopes are $0.5295 \pm 0.0009$ and $-0.5937 \pm 0.0019$, respectively. With the aid of the critical exponents of the system at $\Delta = 1$, we can relate the scaling of the entanglement jet to the corresponding scaling of the density of defects in a Kibble-Zurek type of analysis:

$$d_{\mathrm{KZ}} \propto \frac{a_0}{\xi_0} \left(\tau_0 v\right)^{1/2}, \tag{5}$$

where $a_0$, $\xi_0$, $\tau_0$ are the characteristic length scale, correlation length, and relaxation rate of the system. Note that a KZ-analysis has a limited validity at the phase transition at the $\Delta = 1$ critical point is of BKT type instead of a second-order one.

## S6. NONEQUILIBRIUM QFI IN PRESENCE OF NEXT-NEAREST-NEIGHBOR INTERACTIONS

Finally, we corroborate the stability (or universality) of the nonequilibrium QFI features by also considering the role of additional interactions, that break integrability in the infinite system [7]. We specifically study the dynamical QFI for the spinless fermion chain at half-filling (Eq. (1)) with the inclusion of next-nearest-neighbor interactions of the form $\hat{\mathcal{H}}_{(2)} = V^{(2)} \sum_l \tilde{n}_l \tilde{n}_{l+2}$. The results presented in Fig. S6c for a second-order coupling of $V^{(2)} = 2$ illustrate that the main traits of the nonequilibrium QFI dynamics are preserved. Importantly, this observation underscores the generic character and robustness of our main findings and suggests that they should be observable across many different experimental platforms, irrespective of microscopic details.

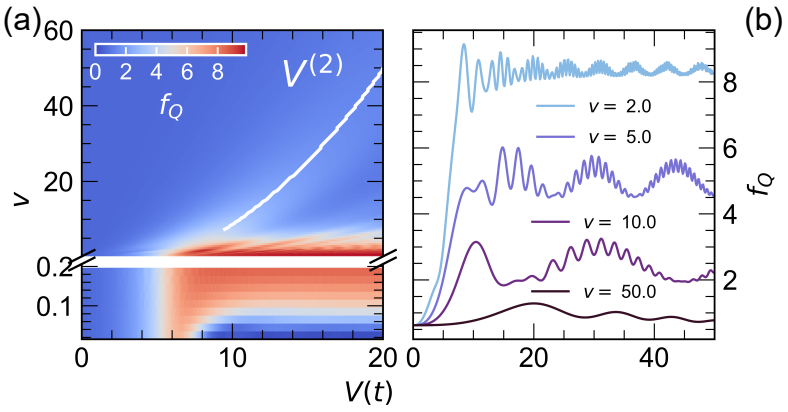


FIG. S6. (a) Non-equilibrium QFI for a Heisenberg chain featuring additional next-nearest neighbour interaction term $\hat{\mathcal{H}}_{(2)}$ as a function of the nearest-neighbour Coulomb repulsion and the ramp speed. (b) Selected 1D line cuts for several ramp velocities.


[1] T. Giamarchi, *Quantum physics in one dimension*, International series of monographs on physics (Clarendon Press, Oxford, 2004).

[2] P. Weinberg and M. Bukov, QuSpin: a Python Package for Dynamics and Exact Diagonalisation of Quantum Many Body Systems. Part I: spin chains, SciPost Phys. **2**, 003 (2017).

[3] P. Weinberg and M. Bukov, QuSpin: a Python Package for Dynamics and Exact Diagonalisation of Quantum Many Body Systems. Part II: bosons, fermions and higher spins, SciPost Phys. **7**, 20 (2019).

[4] M. Kawamura, K. Yoshimi, T. Misawa, Y. Yamaji, S. Todo, and N. Kawashima, Quantum lattice model solver HΦ, Computer Physics Communications **217**, 180 (2017).

[5] D. M. Kennes, A. de la Torre, A. Ron, D. Hsieh, and A. J. Millis, Floquet Engineering in Quantum Chains, Phys. Rev. Lett. **120**, 127601 (2018).

[6] P. Hauke, M. Heyl, L. Tagliacozzo, and P. Zoller, Measuring multipartite entanglement through dynamic susceptibilities, Nature Publishing Group **12**, 778 (2016).

[7] K. Patrick, V. Caudrelier, Z. Papić, and J. K. Pachos, Interaction distance in the extended xxz model, Phys. Rev. B **100**, 235128 (2019).